

Asymmetric Selectivity of Synthetic Conical Nanopores Probed by Reversal Potential Measurements

J. Cervera,[†] A. Alcaraz,[†] B. Schiedt,[‡] R. Neumann,[‡] and P. Ramírez*,[§]

Departamento de Física, Universitat Jaume I, Apartado de Correos 224, E-12080 Castelló, Spain, Gesellschaft für Schwerionenforschung (GSI), Planckstrasse 1, D-64291 Darmstadt, Germany, and Departamento de Física Aplicada, Universidad Politécnica de Valencia, Camino de Vera s/n, E-46022 Valencia, Spain

Received: March 8, 2007; In Final Form: June 5, 2007

The study of rectifying systems like conical nanopores demands an extension of our understanding of ionic selectivity. The asymmetric conduction shown by these pores is connected to the idea of directionality: the rates of ionic transport and the charge regulation exerted by the system are nonsymmetrical. As a result, ionic selectivity is not only a property of the nanopore itself but also depends crucially on the direction of the concentration gradient. Previous studies of current–voltage curves provide an adequate description of the conductive properties of the system but give only indirect clues about how charge regulation is performed. In this sense, the study of the reversal potential offers additional and essential information. To this end, here we present a model for reversal potential in conical nanopores based on the Poisson and Nernst–Planck (PNP) equations. The theoretical results are compared with experimental data, and good agreement is found using only one fitting parameter, the surface charge density, which is determined independent of the current–voltage characteristics.

I. Introduction

Nanoporous materials have outstanding technological applications in catalysis, sensing, and filtration of molecules of size comparable to the pore diameter,^{1–24} and thus there is an increasing interest in the development of new methods able to produce such materials.^{6,25–30} A widely used technique for the production of nanopores is ion track etching,^{31–33} which is based on the irradiation of polymer films with energetic heavy ions, followed by chemical etching of the latent tracks—damaged regions that are created along the ion trajectories. In most polymers, a consequence of the etching process is the generation of negative carboxyl groups (COO[−]) fixed to the pore surface that provide these nanopores with their characteristic cationic selectivity.^{28,31–39} Although the pore density is varied by ion irradiation, the pores' shape and ionic transport properties can be controlled via the etching process and subsequent modification of the pore surface, for example, by deposition of a gold cladding on the inner pore wall and subsequent chemisorption of ion exchange thiols on the gold.^{1–3,20,26,28,39–45} In this context, anisotropic etching and electroless Au plating procedures have been used to produce polymer foils containing a *single* conical nanopore.^{15,26,28,32,34–37,39,44}

Membranes containing a single nanopore generated with the above techniques have emerged as promising materials to mimic biological ion channels.^{15,31,46} The latter are protein structures in cell membranes that are used by the cell to communicate with the external environment and control a large number of physiological processes. Synthetic nanopores as well as biochannels support and regulate the transport of ionic or molecular species through the cell membrane and display a wide range of

permeability profiles, from general diffusion porins to solute specific channels.^{15,28,31,38,47–49} Besides ionic selectivity, synthetic conical nanopores are also able to mimic other distinctive properties found in biological ion channels such as current rectification,^{14,15,32,34–37} flux inhibition by protons and divalent cations,^{31,34,44,47,50–52} transport of ions against concentration gradients,⁵³ and ion current fluctuations.^{28,54} The ability to artificially replicate biological nanosystems is illustrated in recent studies showing how a nonspecific weakly selective channel like OmpF porin can be artificially engineered to behave like a specific highly selective calcium channel.⁵⁵

It has been demonstrated experimentally that the mechanism responsible for the permselectivity is the electrostatic interaction of mobile ions with the pore surface charges, as has also been recognized by most of the existing models for ion transport through conical nanopores.^{14,15,28,38,56–62} In a recent paper,¹⁵ Siwy et al. have described the asymmetric ionic diffusion through synthetic conical nanopores in terms of the electric current measured under zero transmembrane potential when the nanopore separates two electrolyte solutions at different concentrations. Their results were interpreted in terms of a semiquantitative theoretical model based on the Smoluchowski equation,^{15,61} and the authors were able to explain most of the observed phenomena using the diffusion coefficients of the ionic species as fitting model parameters.

In this paper, we focus on the study of the reversal potential in conical nanopores. Reversal potential is defined as the potential at which the current is zero under a concentration gradient. It is therefore closely related to the asymmetric diffusion addressed by Siwy et al.¹⁵ but, as we will see later, permits the characterization of the nanopore selectivity via the ionic transport numbers and allows a deeper investigation of the basic mechanisms involved in ionic transport. Moreover, recent studies of asymmetric ion transport in biological ion channels have been performed in terms of this quantity (see for

* Corresponding author. E-mail: patraho@fis.upv.es.

[†] Universitat Jaume I.

[‡] Gesellschaft für Schwerionenforschung (GSI).

[§] Universidad Politécnica de Valencia.

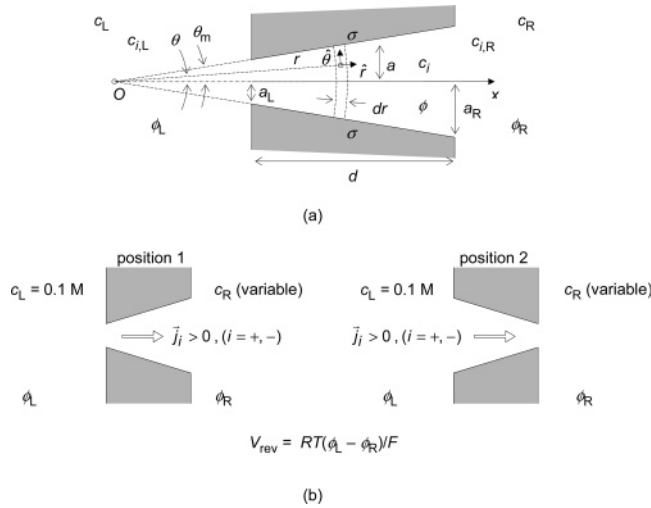


Figure 1. (a) Sketch of the conical nanopore under study. The meaning of the different symbols is detailed in the text. (b) Scheme indicating the two possible positions of the nanopore: the pore tip facing the left chamber (position 1) and the pore tip facing the right chamber (position 2). Sign criteria for the electric potential and the ionic fluxes are also indicated.

example ref 49). For this purpose, we first present a theoretical model aiming to describe quantitatively the reversal potential of conical nanopores. The model is based on the Poisson and Nernst–Planck (PNP) equations and allows the calculation of the profile of average electric potential along the pore as well as the total ionic flux and the transport number of cations. Second, we compare the theoretical predictions with experimental measurements performed under a wide range of salt concentrations. The comparison of theory with experiments provides new insight into the transport phenomena in these nanostructures.

II. Theory

A schematical view of the system under study is shown in Figure 1a. A polymer film containing a single conical nanopore separates two electrolyte solutions (KCl in our case) at concentrations c_k ($k = L$ for the left solution and $k = R$ for the right solution). The pore wall is assumed to contain fixed charge groups homogeneously distributed on the pore surface, σ being the surface charge density. The pore thickness is expressed by d , and its radius a increases linearly from a_L at the left to a_R at the right aperture. θ_m is the pore angle ($\tan \theta_m = (a_R - a_L)/d$). ϕ_k denotes the dimensionless electric potential in the bulk of the solution of chamber k ($k = L, R$). $c_{i,k}$ stands for the concentration of species i ($i = +$ for K^+ and $i = -$ for Cl^-) in the bulk of solution k ($k = L, R$). c_i ($i = +, -$) and ϕ denote, respectively, the local concentration of species i and the local dimensionless electric potential. The system is assumed to be isothermal, at steady state, and free of convective movements.

The two possible positions of the nanopore are shown in Figure 1b. In the following, superscripts (1) and (2) will denote these positions: (1) when the pore tip is faced to the left chamber and (2) when the pore tip is faced to the right chamber. In the theoretical calculations as well as in the measurements, the concentration of KCl in the left chamber will be fixed to $c_L = 0.1$ M. The concentration of KCl in the right chamber will be varied between 0.001 and 3 M in the calculations and between 0.01 and 1 M in the experiments. The potential difference between the solutions in chambers L and R is defined as $V \equiv RT(\phi_L - \phi_R)/F$, where R , T , and F have their usual meaning,

and the ionic flux densities \vec{j}_i ($i = +, -$) flowing from left to right are assumed to be positive.

We will discuss our experimental results on the basis of a theoretical model for ionic transport in conical nanopores developed previously.^{59,62} Briefly, this model assumes that the basic equations describing the ionic transport through the nanopore are the Nernst–Planck equations

$$\vec{j}_i = -D_i(\nabla c_i + z_i c_i \nabla \phi), \quad i = +, - \quad (1)$$

the Poisson equation

$$\nabla^2 \phi = \frac{F^2}{\epsilon RT} (c_- - c_+) \quad (2)$$

and the continuity equation

$$\nabla \cdot \vec{j}_i = 0, \quad i = +, - \quad (3)$$

where z_i is the charge number of ionic species i , and ϵ is the dielectric permittivity of the solution within the pore.

Equations 1–3 can be solved approximately using spherical coordinates with the origin in the cone apex as shown in Figure 1a. Assuming that the ionic flux densities have only radial components

$$\vec{j}_i = j_i \hat{r}, \quad i = +, - \quad (4)$$

and applying the averaging operator

$$\langle \rangle \equiv \frac{1}{(1 - \cos \theta_m)} \int_0^{\theta_m} d\theta \sin \theta \quad (5)$$

to eqs 1–3, we find

$$\frac{d}{dr} (r^2 \langle j_i \rangle) = \frac{d}{dr} \left[-r^2 D_i \left(\frac{d \langle c_i \rangle}{dr} + z_i \langle c_i \rangle \frac{d \langle \phi \rangle}{dr} \right) \right] = 0, \quad i = +, - \quad (6)$$

$$\frac{1}{r^2} \frac{d}{dr} \left(r^2 \frac{d \langle \phi \rangle}{dr} \right) = \frac{F^2}{\epsilon RT} (\langle c_- \rangle - \langle c_+ \rangle - X) \quad (7)$$

where

$$X = \frac{\sin \theta_m \sigma}{Fr(1 - \cos \theta_m)} \quad (8)$$

is the volume fixed charge concentration (with its sign) contained in the differential spherical shell of radius r of Figure 1a (see refs 59 and 62 for more details).

The boundary values for the average ionic concentrations and electric potential at the pore borders, $r = r_L$ and $r = r_R$, are obtained assuming Donnan equilibrium and electroneutrality,⁶³ and yield

$$\langle c_i \rangle_k \equiv \langle c_i(r_k) \rangle = \frac{1}{2} (-z_i X_k + \sqrt{X_k^2 + 4c_k^2}), \quad i = +, -; k = L, R \quad (9)$$

and

$$\langle \phi(r_k) \rangle = \phi_k - \frac{1}{z_i} \ln \frac{\langle c_i \rangle_k}{c_k}, \quad i = +, -; k = L, R \quad (10)$$

where $X_k \equiv X(r_k)$, $k = L, R$.

Solution of eqs 6 and 7 with the boundary conditions in eqs 9 and 10 gives the average profiles of ionic concentration, ionic flux density, and electric potential at any applied V . Integration

of the ionic flux densities through any spherical section of the nanopore gives the total ionic fluxes

$$\langle J_i \rangle = 2\pi(1 - \cos\theta_m)r^2\langle j_i \rangle, \quad i = +, - \quad (11)$$

passing through the nanopore. From these fluxes, the electric current

$$I = \sum_i z_i F \langle J_i \rangle \quad (12)$$

flowing through the pore can be computed.

The reversal potential, V_{rev} , is defined as the potential difference measured between the left and right solutions under zero current conditions and can be obtained by imposing $I = 0$ in the I - V curve of eq 12. This condition leads to

$$\langle J_+ \rangle = \langle J_- \rangle \equiv \langle J \rangle \quad (13)$$

and therefore

$$\langle j_+ \rangle = \langle j_- \rangle \equiv \langle j \rangle \quad (14)$$

According to the scheme shown in Figure 1a, V_{rev} can be split into three terms

$$V_{\text{rev}} = V_{\text{D,L}} + V_{\text{Diff}} + V_{\text{D,R}} \quad (15)$$

The first and third terms of the right-hand side of eq 15 are, respectively, the Donnan potential differences at the left and right pore/solution interfaces and can be calculated from eqs 9 and 10, yielding

$$V_{\text{D,L}} = \frac{RT}{F} [\phi_L - \langle \phi(r_L) \rangle] = \frac{RT}{F} \ln \frac{\langle c_+ \rangle_L}{c_L} = \frac{RT}{F} \ln \frac{-X_L/2 + \sqrt{(X_L/2)^2 + c_L^2}}{c_L} \quad (16)$$

$$V_{\text{D,R}} = \frac{RT}{F} [\langle \phi(r_R) \rangle - \phi_R] = \frac{RT}{F} \ln \frac{c_R}{\langle c_+ \rangle_R} = \frac{RT}{F} \ln \frac{c_R}{-X_R/2 + \sqrt{(X_R/2)^2 + c_R^2}} \quad (17)$$

The second term of the right-hand side of eq 15 is usually called the diffusion potential and corresponds to the electric potential difference that appears within the nanopore

$$V_{\text{Diff}} = \frac{RT}{F} [\langle \phi(r_L) \rangle - \langle \phi(r_R) \rangle] \quad (18)$$

This term can be calculated from the average electric potential profile obtained after integration of eqs 6, 7, and 14.

Two limiting cases will be examined in the following paragraphs. For highly charged pores and very dilute solutions ($|X| \gg c_k$, $k = \text{L, R}$), the ion flux densities are negligible. Substitution of $\langle j \rangle = \langle j_+ \rangle \approx 0$ in eq 6 and further integration between the pore borders give

$$V_{\text{Diff}} \approx \frac{RT}{F} \ln \frac{\langle c_+ \rangle_R}{\langle c_+ \rangle_L} \quad (19)$$

and the reversal potential yields the well-known Nernstian limit (ideal selectivity) that physically corresponds to the total exclusion of coions

$$V_{\text{rev}} \approx \frac{RT}{F} \ln \frac{c_R}{c_L} \quad (20)$$

For weakly charged pores ($|X| \approx 0$), the concentrations of cations and anions within the pore are approximately equal. Substituting $\langle c_+ \rangle = \langle c_- \rangle \equiv \langle c \rangle$ in eq 6 and taking into account that the Donnan potential differences vanish in this limit, the total ionic flux takes the form

$$\langle J \rangle = 4\pi \frac{1 - \cos\theta_m}{\sin\theta_m} \frac{D_+ D_-}{D_+ + D_-} \frac{a_L a_R}{a_L - a_R} (c_L - c_R) \quad (21)$$

and the reversal potential gives the liquid junction limit⁶³

$$V_{\text{rev}} = V_{\text{Diff}} = -\frac{RT}{F} \frac{D_- - D_+}{D_- + D_+} \ln \frac{c_R}{c_L} \quad (22)$$

Figures 2–11 show the results provided by the above theoretical model using $a_L = 5$ nm, $a_R = 200$ nm, $T = 293$ K, and $\epsilon = 80 \epsilon_0$, where ϵ_0 is the electric permittivity of vacuum, and the (infinite dilution) diffusion coefficients of the ionic species $D_+ = 1.95 \cdot 10^{-5}$ cm²/s (K^+) and $D_- = 2.03 \cdot 10^{-5}$ cm²/s (Cl^-).⁶⁴ c_L was fixed to 0.1 M KCl, and c_R was varied from 0.001 M up to 3 M KCl. The results shown in Figures 2–6 correspond to the relatively high fixed charge concentration $\sigma = -1$ e/nm², where e is the elementary charge, and those in Figures 7–11 correspond to the relatively low fixed charge concentration $\sigma = -0.1$ e/nm².

Figure 2 shows the reversal potential of the conical nanopore versus $\log(c_R/c_L)$. Diagrams on the right side illustrate the two possible positions of the pore. The black curves represent the numerical solutions provided by the above theoretical model for $I = 0$ (continuous line for position 1 and dashed line for position 2, and the dotted–dashed curve correspond to the Nernst limit given in eq 20. Because the pore fixed charge density is relatively high in this case, the Nernst limit constitutes a good approximation of the reversal potential for $c_R < c_L = 0.1$ M. For $c_R > c_L$, the values calculated for the nanopore are smaller than the Nernst limit because the nanopore selectivity decreases as the concentrations used here are relatively high and screen the charges on the pore walls. When we compare the numerical solutions obtained for positions 1 and 2, we find that major differences between the two positions appear for $c_R > c_L$. The curve corresponding to position 1 shows that $V_{\text{rev}}^{(1)}$ increases monotonically with $\log(c_R/c_L)$, whereas $V_{\text{rev}}^{(2)}$ attains a maximum value at $c_R \approx 0.5$ M.

The asymmetry of the reversal potential becomes evident in Figure 3 for $\Delta V_{\text{rev}} \equiv V_{\text{rev}}^{(1)} - V_{\text{rev}}^{(2)}$ versus $\log(c_R/c_L)$. For $c_R \ll c_L = 0.1$ M, both $V_{\text{rev}}^{(1)}$ and $V_{\text{rev}}^{(2)}$ are negative and, because $|V_{\text{rev}}^{(2)}| > |V_{\text{rev}}^{(1)}|$, ΔV_{rev} attains a positive, small limiting value close to 2 mV (calculations not shown here indicate that this limiting value tends to zero with increasing $|\sigma|$, as would be the case for an ideally selective pore where both $V_{\text{rev}}^{(1)}$ and $V_{\text{rev}}^{(2)}$ tend to the Nernstian limit of eq 20.) On the contrary, for $c_R > c_L$ $V_{\text{rev}}^{(1)}$ and $V_{\text{rev}}^{(2)}$ are positive and $V_{\text{rev}}^{(1)} > V_{\text{rev}}^{(2)}$. Thus, ΔV_{rev} increases rapidly with c_R and gives $\Delta V_{\text{rev}} \approx 20$ mV at $c_R = 1$ M. Interestingly, this value is on the same order as those observed in some asymmetric biological pores, where, for instance, we have measured $\Delta V_{\text{rev}} \approx 22$ mV at $c_L = 0.1$ M KCl and $c_R = 1$ M KCl in the case of the ion channel meningococcal PorA/C1 from *Neisseria Meningitidis*.

To allow a more detailed interpretation of the results in Figures 2 and 3, we have calculated the profiles of the electrical

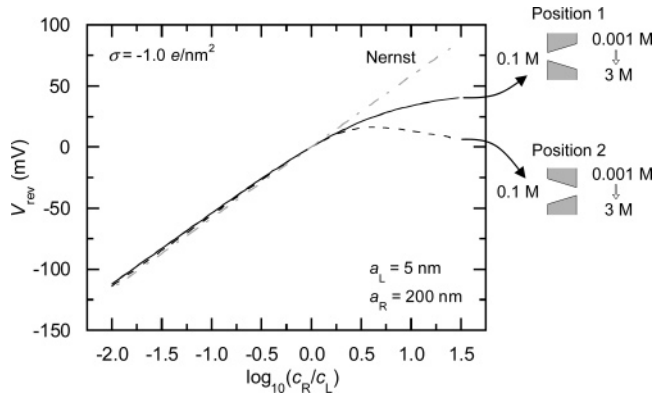


Figure 2. Calculated reversal potential vs $\log(c_R/c_L)$ for a conical nanopore with pore radii $a_L = 5$ nm, $a_R = 200$ nm, and fixed charge concentration $\sigma = -1$ e/nm². c_L was fixed to 0.1 M, and c_R was varied from 0.001 up to 3 M. The curves represent the Nernst limit (dotted-dashed curve), and the numerical solutions provided by the theoretical model: position 1 (continuous curve), position 2 (dashed curve).

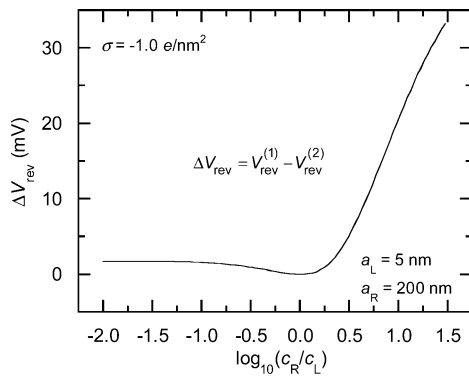


Figure 3. Calculated values of $\Delta V_{\text{rev}} \equiv V_{\text{rev}}^{(1)} - V_{\text{rev}}^{(2)}$ vs $\log(c_R/c_L)$ for the conical nanopore of Figure 2.

potential versus the coordinate x along the pore symmetry axis. We have considered the cases $c_R = 0.1$ M (Figure 4a), 0.01 M (Figure 4b), and 1 M (Figure 4c), and fixed the arbitrary origin $\phi_R = 0$ for the electric potential at the right external solution. In each case, the results corresponding to position 1 (continuous curves) and position 2 (dashed curves) have been plotted. The vertical arrows on the left of Figure 4b and c give the reversal potential for the two positions (note the different scales of the ordinate axes in a–c). The steps at the pore borders ($x = 0$ and $x = 12$ μm) correspond to the Donnan contributions to the reversal potential. The depth of each step is determined by the concentrations of the fixed charges and the bathing solution (see eqs 16 and 17.) In all cases, the electric potential profiles shows a clear, characteristic potential well at the pore tip.^{38,59} In Figure 4a, no concentration gradient is applied to the nanopore ($c_L = c_R = 0.1$ M) and therefore $V_{\text{rev}}^{(1)} = V_{\text{rev}}^{(2)} = 0$ (note that any other result different from zero at these concentrations would violate the second law of thermodynamics). As a consequence, $V_{\text{Diff}}^{(1)} = -V_{\text{D,L}}^{(1)} - V_{\text{D,R}}^{(1)} = -V_{\text{D,L}}^{(1)}$ (this is a particular characteristic of the asymmetric pore because a symmetric one would give $V_{\text{Diff}} = 0$), the potential profiles for positions 1 and 2 are completely symmetrical and therefore $\Delta V_{\text{rev}} = 0$, giving the minimum of Figure 3. The potential profiles become asymmetric for $c_L \neq c_R$. In Figure 4b, both $V_{\text{rev}}^{(1)}$ and $V_{\text{rev}}^{(2)}$ give values close to the Nernstian limit because of the effect of the fixed charges that efficiently exclude the coions. Finally, Figure 4c reveals that $|V_{\text{D,L}}^{(1)}| \gg |V_{\text{D,L}}^{(2)}|$, and therefore $V_{\text{rev}}^{(1)} \gg V_{\text{rev}}^{(2)}$, as a consequence of the screening of the right Donnan potential difference of position 2 when the concentrated solution faces the pore tip. Therefore,

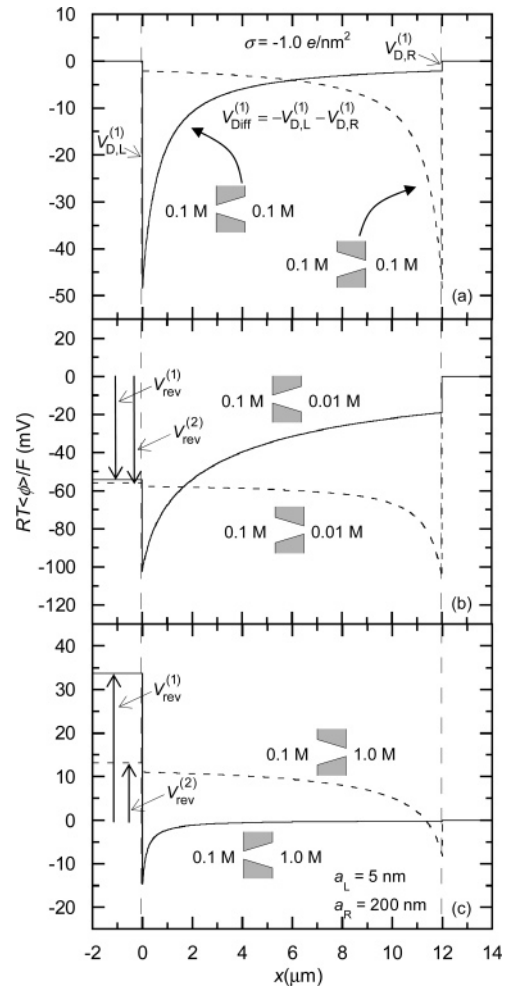


Figure 4. Calculated profiles of electrical potential vs the coordinate x along the pore symmetry axis for the conical nanopore of Figures 2 and 3 in the cases $c_R = 0.1$ M (a), 0.01 M (b), and 1 M (c). The continuous curves correspond to position 1, and the dashed curves correspond to position 2 in Figure 1b.

it can be concluded that the charge regulation at the cone tip for position 2 is the origin of the asymmetry in the reversal potential seen in Figures 2 and 3 for $c_R > c_L$.

The properties of the reversal potential discussed above are also connected with the ionic fluxes through the nanopore. Figure 5a shows the total ionic flux passing through the nanopore versus $\log(c_R/c_L)$. Because the driving force responsible for the ionic flux is the concentration gradient applied to the nanopore, both $\langle J \rangle^{(1)}$ and $\langle J \rangle^{(2)}$ are positive for $c_R < c_L$, zero for $c_R = c_L$, and negative for $c_R > c_L$, according to the sign criteria shown in Figure 1b. A closer inspection of the results obtained reveals that $\langle J \rangle^{(1)} \geq \langle J \rangle^{(2)} \approx 0$ for $c_R < c_L$, as expected from the validity of the Nernstian limit. On the contrary, we see that $|\langle J \rangle^{(2)}| > |\langle J \rangle^{(1)}|$ for $c_R > c_L$, and also that both $|\langle J \rangle^{(1)}|$ and $|\langle J \rangle^{(2)}|$ increase rapidly as c_R increases. Figure 5b shows the calculated values of $\Delta \langle J \rangle \equiv \langle J \rangle^{(1)} - \langle J \rangle^{(2)}$ versus $\log(c_R/c_L)$. Interestingly, we find that $\Delta \langle J \rangle$ follows exactly the same trends that ΔV_{rev} (compare Figures 3 and 5b).

A quantitative measure of the pore selectivity is the transport number for cations,⁶³ defined as

$$t_+ \equiv \frac{1}{2} \left[1 + \frac{F}{RT} \frac{V_{\text{rev}}}{\ln(c_R/c_L)} \right] \quad (23)$$

The transport number (transference number), representing the fraction of the total current carried by an ion in a particular

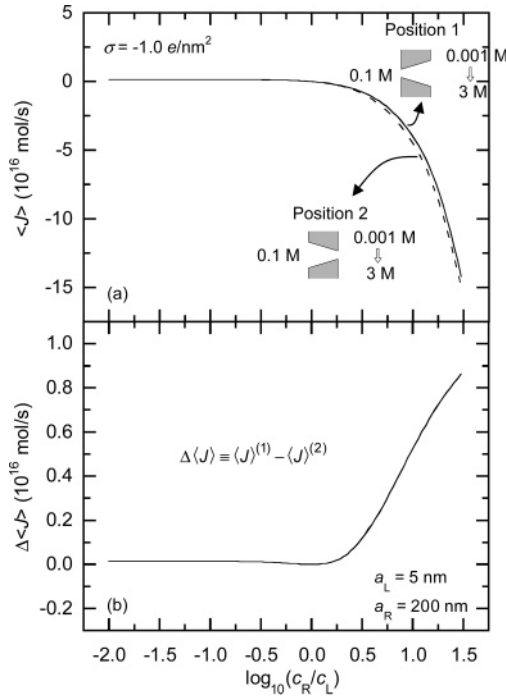


Figure 5. (a) Total ionic flux passing through the nanopore of Figures 2 and 3 vs $\log(c_R/c_L)$. The continuous curve corresponds to position 1, and the dashed curve corresponds to position 2. (b) Calculated values of $\Delta \langle J \rangle \equiv \langle J \rangle^{(1)} - \langle J \rangle^{(2)}$ vs $\log(c_R/c_L)$ for the same nanopore.

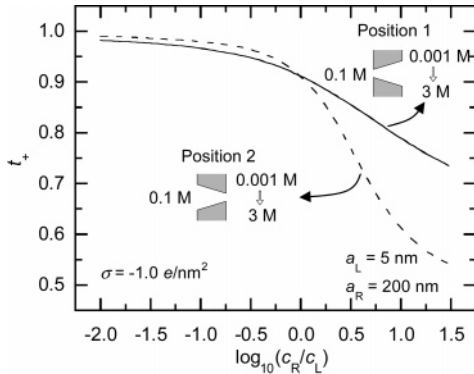


Figure 6. Calculated values of the transport number of cations vs $\log(c_R/c_L)$ for the conical nanopore of Figures 2–5.

phase constitutes the natural connection between the I – V curves and the reversal potential measurements. The t_+ ranges between two limiting values. In the case of uncharged pores ($\sigma \rightarrow 0$), the pore exhibits no selectivity. Substituting eq 22 in eq 23, we find the lower limit for t_+

$$t_+(\sigma \rightarrow 0) = \frac{1}{2} \left[1 - \frac{D_- - D_+}{D_- + D_+} \right] \quad (24)$$

In the case of KCl, we obtain $t_+(\sigma \rightarrow 0) = 0.49$. On the contrary, when the fixed charge density is very high ($\sigma \rightarrow +\infty$) the pore behaves as an ideally selective one, allowing no coion to enter the pore, and the reversal potential yields the Nernstian value given in eq 20. Substitution of this value in eq 23 gives the upper limit for t_+

$$t_+(\sigma \rightarrow +\infty) = 1 \quad (25)$$

regardless of the electrolyte used. Therefore, in the case of nanopores selective to cations and using KCl as electrolyte, the transport number of K^+ ranges from 0.49 to 1.

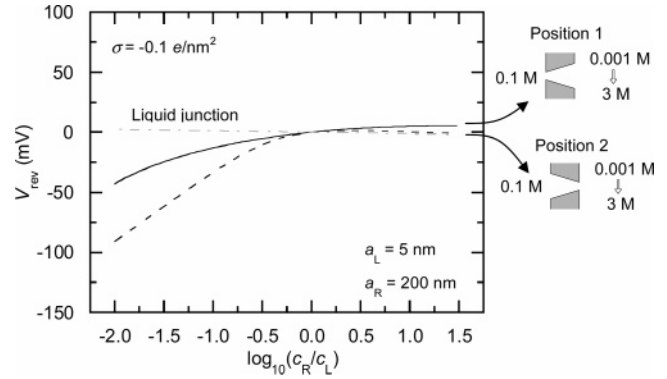


Figure 7. Calculated reversal potential vs $\log(c_R/c_L)$ for a conical nanopore with pore radii $a_L = 5 \text{ nm}$, $a_R = 200 \text{ nm}$ and fixed charge concentration $\sigma = -0.1 \text{ e/nm}^2$. c_L was fixed to 0.1 M, and c_R was varied from 0.001 up to 3 M. The curves represent the liquid junction limit (dotted–dashed curve) and the numerical solutions provided by the theoretical model: position 1 (continuous curve), position 2 (dashed curve).

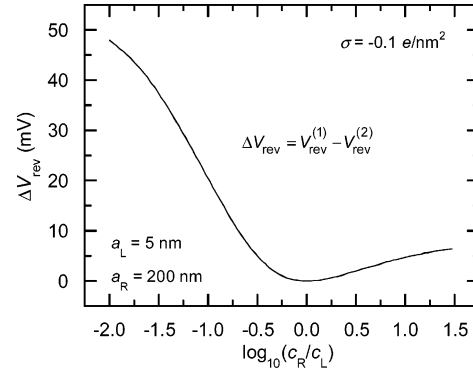


Figure 8. Calculated values of $\Delta V_{\text{rev}} \equiv V_{\text{rev}}^{(1)} - V_{\text{rev}}^{(2)}$ vs $\log(c_R/c_L)$ for the conical nanopore of Figure 7.

In our case, because the fixed charges attached to the pore surface are negative, the nanopore is expected to be selective to cations. The calculated values of t_+ versus $\log(c_R/c_L)$ for the same pore as in Figures 2–5 have been plotted in Figure 6. Again, the continuous curve refers to position 1 and the dashed one refers to position 2. As expected, we see that $0.49 < t_+ < 1$ for the two positions of the nanopore in the whole range of $\log(c_R/c_L)$. For $c_R \ll c_L$, the selectivity attains values close to 1, and the nanopore behaves in this limit as an ideally selective pore (note that the fixed charge density used in the calculations is relatively high). It can be observed how the physical picture behind t_+ close to 1 is exactly the same as the Nernstian limit for the reversal potential: the nanopore surface charges prevent coions from entering the pore so that only counterions contribute to the total current. No asymmetry is found between both positions 1 and 2, meaning that in both orientations the charge at the nanopore mouth is high enough to provide an effective exclusion of negative chloride ions. We see also that t_+ decreases as c_R increases, as a consequence of the better screening of the fixed charges when the number of mobile ions within the pore is increased.

There is a clear correspondence between the pore selectivity and the total ion flux (compare Figures 5a and 6): for $c_R < c_L$ the pore selectivity is high, but mobile ions are excluded from the pore by the fixed charges and, as a result, the total ion flux is small. For $c_R > c_L$ the number of mobile ions within the pore is increased and the absolute value of the ion flux increases accordingly, but the prize to be paid is a loss of selectivity. This relationship is observed again when the curves correspond-

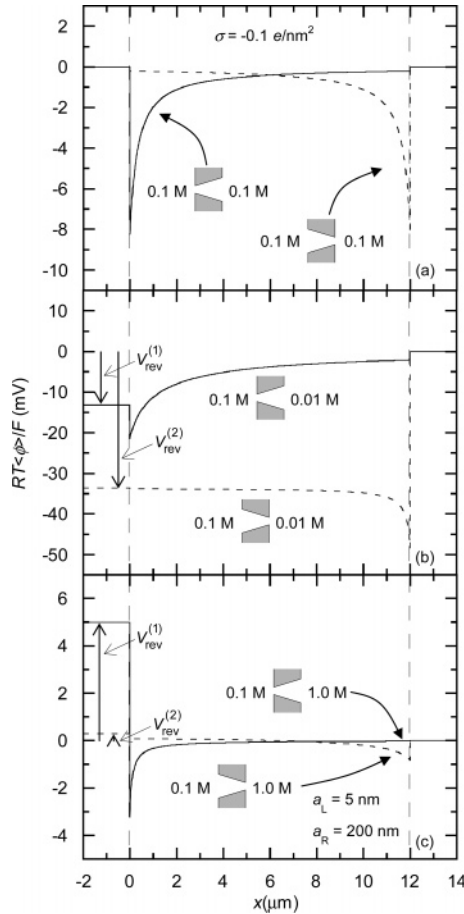


Figure 9. Calculated profiles of electrical potential vs the coordinate x along the pore symmetry axis for the conical nanopore of Figures 7–9 in the cases $c_R = 0.1$ M (a), 0.01 M (b), and 1 M (c). The continuous curves correspond to position 1, and the dashed curves correspond to position 2.

ing to positions 1 and 2 are compared. We see that $t_+^{(2)} > t_+^{(1)}$ for $c_R < c_L$ and $t_+^{(1)} > t_+^{(2)}$ for $c_R > c_L$. From Figure 5b, it can be seen that in the former case the total ion flux for position 1 is (slightly) higher, whereas for $c_R > c_L$ it is higher for position 2. Thus, we see that the pore selectivity (as well as the reversal potential) is higher, and therefore the total ion flux is smaller, when the low concentration faces the pore tip and the mobile carriers screen the fixed charges.

The results shown in Figures 7–11 correspond to the relatively low fixed charge concentration $\sigma = -0.1$ e/nm². Figure 7 shows the reversal potential of the conical nanopore versus $\log(c_R/c_L)$. This plot is to be compared with Figure 2. Again, the continuous curve corresponds to position 1, and the dashed one corresponds to position 2. The dotted–dashed curve now refers to the liquid junction limit given in eq 22. We see that the numerical calculations now attain lower values than those of Figure 2 and deviate from the Nernst limit, as a consequence of the relatively low fixed charge density used in the calculations. In the limit $c_R > c_L$, the numerical results of V_{rev} for the two positions are close to the liquid junction limit given in eq 22. As a consequence, comparison of the numerical solutions obtained for positions 1 and 2 reveals that major differences between the two positions now appear for $c_R < c_L$. These differences are better seen in Figure 8, where $\Delta V_{rev} \equiv V_{rev}^{(1)} - V_{rev}^{(2)}$ versus $\log(c_R/c_L)$ has been plotted. Interestingly, we find that the asymmetry of the reversal potential is even more pronounced for $\sigma = -0.1$ e/nm² and $c_R < c_L$ than for $\sigma = -1$ e/nm² and $c_R > c_L$ (compare Figures 3 and 8).

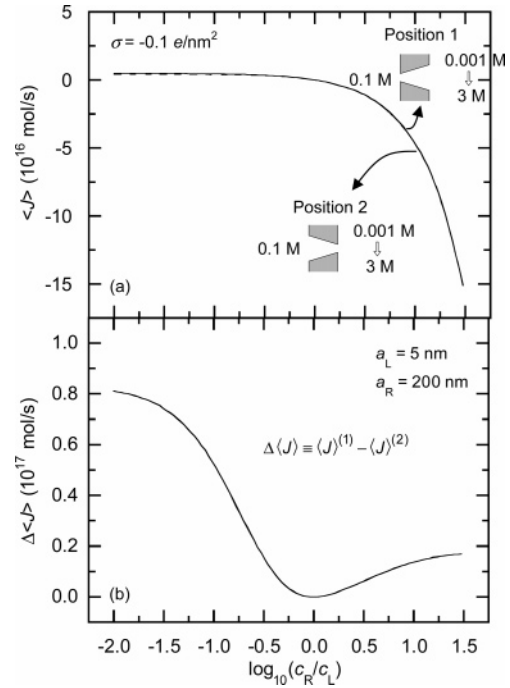


Figure 10. (a) Total ionic flux passing through the nanopore of Figures 7 and 8 vs $\log(c_R/c_L)$. (b) Asymmetry of the ion flux $\Delta \langle J \rangle \equiv \langle J \rangle^{(1)} - \langle J \rangle^{(2)}$ vs $\log(c_R/c_L)$.

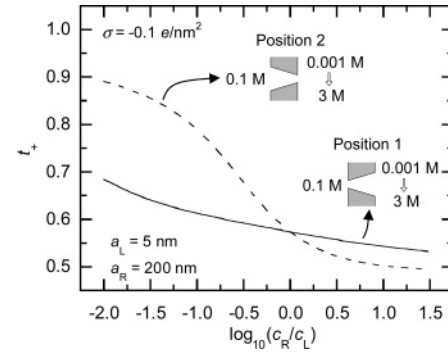


Figure 11. Calculated values of the transport number of cations vs $\log(c_R/c_L)$ for the conical nanopore of Figures 7–10.

Figure 9a–c shows the calculated profiles of electrical potential versus the coordinate x along the pore symmetry axis for the cases $c_R = 0.1$ M (Figure 9a), 0.01 M (Figure 9b), and 1 M (Figure 9c). Again we have plotted the results corresponding to position 1 (continuous curves) and position 2 (dashed curves). The arrows on the left account for the reversal potential. Because the pore fixed charge considered is relatively low, the Donnan potential steps at the pore borders $x = 0$ and $x = 12$ μm (and therefore the potential well at the pore tip) are now smaller than those calculated in the case $\sigma = -1$ e/nm² (compare Figure 4a–c with Figure 9a–c; note the different scales used in the vertical axes). Again, the potential profiles become asymmetric for $c_L \neq c_R$, but we notice in Figure 9b that the main differences between $V_{rev}^{(1)}$ and $V_{rev}^{(2)}$ appear for $c_L = 0.1$ M and $c_y = 0.01$ M. The potential profiles calculated in this case reveal that the Donnan potential difference at the pore tip for position 2, $V_{D,R}^{(2)}$, gives most of the reversal potential calculated in this case (note that now the concentration of fixed charges at the pore tip is small, but the concentration of the electrolyte facing the pore tip is comparatively smaller, and this leads to a relatively high Donnan step). $V_{D,L}^{(1)}$, $V_{D,R}^{(1)}$, and $V_{D,L}^{(2)}$ are small because of screening of the pore fixed charges, and the difference between $V_{rev}^{(1)}$ and $V_{rev}^{(2)}$ is dictated mainly by $V_{D,R}^{(2)}$. For

$c_L = 0.1$ M and $c_R = 1$ M, the results shown in Figure 9c show that, because the concentration of the electrolyte facing the pore tip is high when compared to the concentration of fixed charges, the Donnan potential differences at the pore borders are small, and therefore the difference between $V_{\text{rev}}^{(1)}$ and $V_{\text{rev}}^{(2)}$ is also small.

The plots of total ionic flux passing through the nanopore versus $\log(c_R/c_L)$ shown in Figure 10a present trends similar to those observed in the case $\sigma = -1$ e/nm² (compare Figure 10a with Figure 5a) in the whole range of $\log(c_R/c_L)$ represented. However, the plot of $\Delta\langle J \rangle \equiv \langle J \rangle^{(1)} - \langle J \rangle^{(2)}$ versus $\log(c_R/c_L)$ shown in Figure 10b indicates that the asymmetry between $|\langle J \rangle^{(1)}|$ and $|\langle J \rangle^{(2)}|$ now appears for $c_R < c_L$, whereas $\Delta\langle J \rangle$ attains small values for $c_R > c_L$. This can be explained easily because both $|\langle J \rangle^{(1)}|$ and $|\langle J \rangle^{(2)}|$ approximate to the total ionic flux given in eq 21.

Figure 11 shows the calculated values of t_+ versus $\log(c_R/c_L)$ for position 1 (continuous curve) and position 2 (dashed curve). We see that the nanopore is still selective to cations in the whole range of $\log(c_R/c_L)$, but the values obtained for t_+ are now much lower than those calculated for $\sigma = -1$ e/nm² (compare Figure 11 with Figure 6), indicating that the nanopore selectivity becomes poorer for the two positions. This is especially noticeable in the case of position 1, where a quasi-linear dependence of $t_+^{(1)}$ with $\log(c_R/c_L)$ is found, showing that the ability of the nanopore to regulate the ion transport in an asymmetric way is almost lost. We also see that the asymmetry in the selectivity of the nanopore now appears for $c_R < c_L$. In this limit, only when the diluted solution faces the cone tip (position 2), the nanopore fixed charges are able to significantly exclude the coions. For $c_R > c_L$, $t_+^{(1)}$ and $t_+^{(2)}$ approximate to the liquid junction limit $t_+(\sigma \rightarrow 0) = 0.49$, meaning that the nanopore charges are insufficient to exert a regulation on the ionic transport and produce current rectification. In spite of these differences, the correspondence between the pore selectivity and the total ion flux found for $\sigma = -1$ e/nm² is again observed: the pore selectivity is higher and the total ion flux smaller when the low concentration faces the pore tip.

III. Experiment

The experimental data were obtained with a single conical nanopore in a polyethylene terephthalate (PET) polymer film (Hostaphan RN12, Hoechst, thickness 12 μm). The film was irradiated at the UNILAC linear accelerator (GSI, Darmstadt) with a single heavy ion (U^{28+}) of energy 11.4 MeV per nucleon. The conical pore was created by etching the irradiated film from one side in a conductivity cell (9 M NaOH) at room temperature, using a stopping solution (1 M KCl + 1 M formic acid) on the opposite side of the membrane to neutralize the etchant in the pore tip immediately after the breakthrough (observed as a sudden occurrence of current through the pore³²). To ensure a nanometer-sized opening on the non-etched membrane side, the voltage used to monitor the etching process was applied in such a way that the active OH^- ions were swept out of the pore. Experiments were performed in a three-chamber cell using unbuffered KCl at $\text{pH } 5.6 \pm 0.2$ to avoid the introduction of additional ionic species into the system. The voltage was applied via Ag|AgCl electrodes with a National Instruments analog I/O card using a triangular signal of frequency 0.005 Hz composed of 50 mV steps.

A previous step needed in the discussion of the experimental results is the estimation of the fixed charge density of the nanopore. The wide pore radius is usually calculated from the bulk etch rate and the time of etching.³⁵ This procedure has been confirmed experimentally by scanning-electron micros-

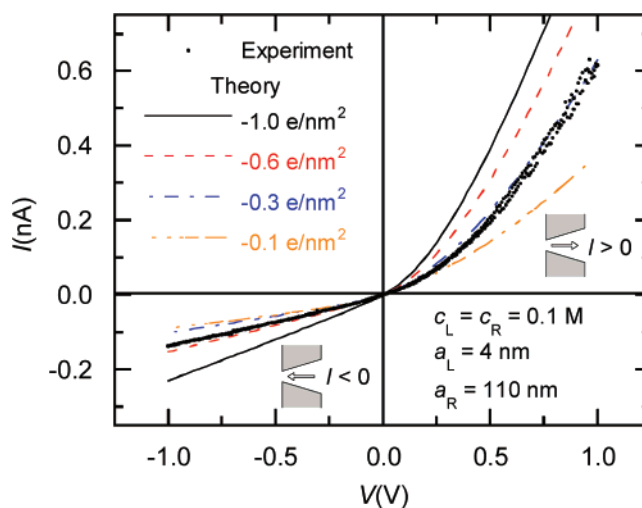


Figure 12. I – V curve of a conical nanopore with pore radii $a_L = 4$ nm and $a_R = 110$ nm under symmetric electrolyte conditions ($c_L = c_R = 0.1$ M). The points correspond to the experimental data, and the continuous curves correspond to the results provided by the theoretical model for $I \neq 0$. The curves are parametric in the surface charge density (e stands for the elementary charge). Best results are obtained using $\sigma = -0.3$ e/nm².

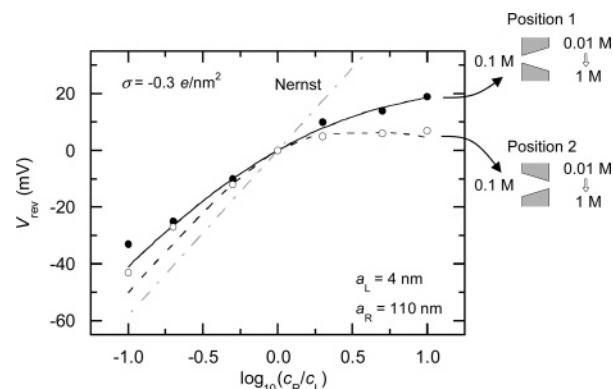


Figure 13. Reversal potential vs $\log(c_R/c_L)$ of the conical nanopore of Figure 12. The results were obtained with $c_L = 0.1$ M KCl, and c_R was varied from 0.01 to 1 M KCl. The points correspond to the experimental data, and the curves correspond to the results provided by the theoretical model using the value $\sigma = -0.3$ e/nm² deduced from Figure 12.

copy.^{35,36} The narrow radius is determined from conductance measurements^{35,36} or using size-exclusion techniques based on pore conductivity in the presence of macromolecules.³⁴ It has been shown recently for somewhat larger (40 nm) pores by SEM that the conductivity method gives reliable values.⁶⁵ In our case, we obtained $a_L = 4$ nm and $a_R = 110$ nm. Therefore, because we use the infinite dilution values for the diffusion coefficients of the ionic species, the only unknown parameter to be introduced in the calculations is σ . Figure 12 shows the I – V curve of the conical nanopore under symmetric electrolyte conditions ($c_L = c_R = 0.1$ M). The points correspond to the experimental data, and the continuous curves to the theoretical results provided by the theoretical model for $I \neq 0$. The curves are parametric in the surface charge density (e stands for the elementary charge). We see that the best agreement between theory and experiment is achieved for $\sigma = -0.3$ e/nm², which is an intermediate value between the two cases studied theoretically in the previous section.

The reversal potential of the same conical nanopore as that in Figure 12 is shown in Figure 13. The points correspond to the experiments (solid circles for position 1 and empty circles for position 2), and the curves to the results provided by the

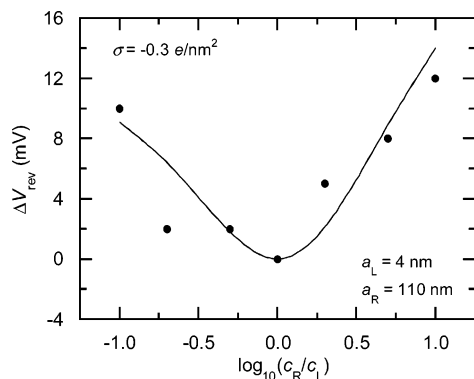


Figure 14. $\Delta V_{\text{rev}} \equiv V_{\text{rev}}^{(1)} - V_{\text{rev}}^{(2)}$ vs $\log(c_{\text{R}}/c_{\text{L}})$ for the conical nanopore of Figures 12 and 13. The points correspond to the experimental data, and the curves correspond to the results provided by the theoretical model using $\sigma = -0.3 \text{ e/nm}^2$.

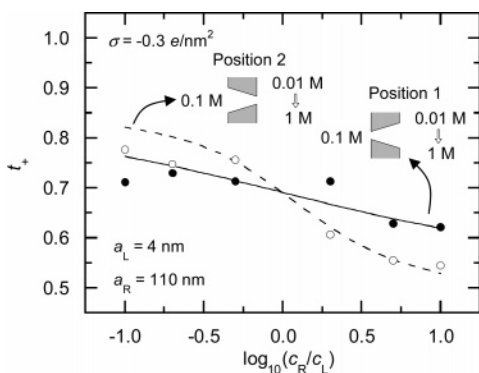


Figure 15. Transport number of cations vs $\log(c_{\text{R}}/c_{\text{L}})$ for the conical nanopore of Figures 12–14. The points correspond to the experimental data, and the curves correspond to the results provided by the theoretical model using $\sigma = -0.3 \text{ e/nm}^2$.

theoretical model (continuous curve for position 1, dashed curve for position 2, and dotted–dashed curve for the Nernst limit). In the experiments, c_{L} was fixed to 0.1 M KCl, and c_{R} was varied from 0.01 to 1 M KCl. The theoretical curves were obtained using the same model parameters as those in Figure 12, and therefore no additional fitting parameters were introduced in the calculations of Figure 13. In spite of this, we find a remarkable agreement between theory and experiment, even though the electrolytes used span 2 orders of magnitude in concentration. We see also that both the experimental and theoretical results share some of the characteristics described in the theoretical section for $\sigma = -1 \text{ e/nm}^2$ and $\sigma = -0.1 \text{ e/nm}^2$, as expected for a nanopore with an intermediate fixed charge concentration: $V_{\text{rev}}^{(1)}$ and $V_{\text{rev}}^{(2)}$ separate from the Nernstian limit and the $V_{\text{rev}}^{(1)}$ curve lies systematically above the $V_{\text{rev}}^{(2)}$ one. It becomes also evident that differences between the two possible positions (Figure 15) now appear for both $c_{\text{R}} < c_{\text{L}}$ and $c_{\text{R}} > c_{\text{L}}$, where we find $\Delta V_{\text{rev}} \approx 9 \text{ mV}$ for $c_{\text{R}} = 0.01 \text{ M}$ and $\Delta V_{\text{rev}} \approx 12 \text{ mV}$ for $c_{\text{R}} = 1 \text{ M}$.

Finally, Figure 15 shows the transport number of cations for the same nanopore as in Figures 12–14. The points represent the experiments (full circles for position 1 and empty circles for position 2), and the curves represent the theoretical results (continuous curve for position 1 and dashed curve for position 2). Again, we find a good agreement between theory and experiments. The latter confirms that $t_+^{(2)} > t_+^{(1)}$ for $c_{\text{R}} < c_{\text{L}}$ but $t_+^{(1)} > t_+^{(2)}$ for $c_{\text{R}} > c_{\text{L}}$. As discussed above, this means that the lower the concentration facing the cone tip, the lower the screening of the fixed charges and, consequently, the higher the selectivity exhibited by the nanopore.

IV. Conclusions

We have presented a theoretical model for the reversal potential in conical nanopores based on the PNP equations. The calculations have been compared with experimental data, and good agreement has been found using only one fitting parameter (the surface charge density σ), which is determined independent of the I – V characteristics. The charge regulation exerted by the system at the pore|external solution interfaces has been identified as the main factor responsible for the asymmetric conduction of the system.

Special attention has been paid to the asymmetries found in the reversal potential when the concentration gradient applied to the nanopore is reversed, heading to the main message of the present paper. In an asymmetric system like the conical one considered here, ion selectivity is not only a property of the system itself but is also connected to the idea of directionality. Thus, the reversal potential depends on the direction of the applied salt gradient, showing that ion selectivity is a consequence of geometric effects and the electrostatic interactions between the nanopore fixed charges and the salt ions. The physical picture beyond this has been explored in a wide range of conditions and can be better understood from the close connection found between reversal potential, total ionic flux, and pore selectivity.

Acknowledgment. We thank Salvador Mafé for fruitful discussions. Also, financial support from Generalitat Valenciana (Project GV04A/701), MEC (Projects FJS2004-03424, MAT2005-01441, and MAT03097), and FEDER, is gratefully acknowledged.

References and Notes

- (1) Martin, C. R. *Science* **1994**, *266*, 1961–1966.
- (2) Nishizawa, M.; Menon, V. P.; Martin, C. R. *Science* **1995**, *268*, 700–702.
- (3) Yu, S.; Lee, S. B.; Kang, M.; Martin, C. R. *Nano Lett.* **2001**, *1*, 495–498.
- (4) Chun, K. -Y.; Stroeve, P. *Langmuir* **2002**, *18*, 4653–4658.
- (5) Steinle, E. D.; Mitchell, D. T.; Wirtz, M.; Lee, S. B.; Young, V. Y.; Martin, C. R. *Anal. Chem.* **2002**, *74*, 2416–2422.
- (6) Chen, P.; Mitsui, T.; Farmer, D. B.; Golovchenko, J.; Gordon, R. G.; Branton, D. *Nano Lett.* **2004**, *4*, 1333–1337.
- (7) Kohli, P.; Wirtz, M.; Martin, C. R. *Electroanalysis* **2004**, *16*, 9–18.
- (8) Lee, S.; Zhang, Y.; White, H. S.; Harrell, C. C.; Martin, C. R. *Anal. Chem.* **2004**, *76*, 6108–6115.
- (9) Ku, J.-R.; Stroeve, P. *Langmuir* **2004**, *20*, 2030–2032.
- (10) Gasparac, R.; Mitchell, D. T.; Martin, C. R. *Electrochim. Acta* **2004**, *49*, 847–850.
- (11) Mara, A.; Siwy, Z.; Trautmann, C.; Wan, J.; Kamme, F. *Nano Lett.* **2004**, *4*, 497–501.
- (12) Stein, D.; Kruthof, M.; Dekker, C. *Phys. Rev. Lett.* **2004**, *93*, 035901.
- (13) Heins, E. A.; Siwy, Z. S.; Baker, L. A.; Martin, C. R. *Nano Lett.* **2005**, *5*, 1824–1829.
- (14) Schiedt, B.; Healy, K.; Morrison, A. P.; Neumann, R.; Siwy, Z. *Nucl. Instrum. Methods Phys. Res., Sect. B* **2005**, *236*, 109–116.
- (15) Siwy, Z.; Kosińska, I. D.; Fuliński, A.; Martin, C. R. *Phys. Rev. Lett.* **2005**, *94*, 048102.
- (16) Fologea, D.; Gershow, M.; Ledden, B.; McNabb, D. S.; Golovchenko, J. A.; Li, J. *Nano Lett.* **2005**, *5*, 1905–1909.
- (17) Fologea, D.; Uplinger, J.; Thomas, B.; McNabb, D. S.; Li, J. *Nano Lett.* **2005**, *5*, 1734–1737.
- (18) Karnik, R.; Fan, R.; Yue, M.; Li, D.; Yang, P.; Majumdar, A. *Nano Lett.* **2005**, *5*, 943–948.
- (19) Plecis, A.; Schoch, R. B.; Renaud, P. *Nano Lett.* **2005**, *5*, 1147–1155.
- (20) Siwy, Z.; Trofin, L.; Kohli, P.; Baker, L. A.; Trautmann, C.; Martin, C. R. *J. Am. Chem. Soc.* **2005**, *127*, 5000–5001.
- (21) Lebedev, K.; Mafé, S.; Stroeve, P. *J. Phys. Chem. B* **2005**, *109*, 14523–14528.
- (22) Choi, Y.; Baker, L. A.; Hillebrenner, H.; Martin, C. R. *Phys. Chem. Chem. Phys.* **2006**, *8*, 4976–4988.

- (23) Chun, K. -Y.; Mafé, S.; Ramírez, P.; Stroeve, P. *Chem. Phys. Lett.* **2006**, *418*, 561–564.
- (24) Ku, J. -R.; Lai, S. -M.; Ileri, N.; Ramírez, P.; Mafé, S.; Stroeve, P. *J. Phys. Chem. C* **2007**, *111*, 2965–2973.
- (25) Matthias, S.; Müller, F. *Nature* **2003**, *424*, 53–57.
- (26) Li, N.; Yu, S.; Harrell, C. C.; Martin, C. R. *Anal. Chem.* **2004**, *76*, 2025–2030.
- (27) Ding, Y.; Kim, Y. -J.; Erlebacher, J. *Adv. Mater.* **2004**, *16*, 1897–1900.
- (28) Siwy, Z. S. *Adv. Funct. Mater.* **2006**, *16*, 735–746.
- (29) Vlasiouk, I.; Siwy, Z. S. *Nano Lett.* **2007**, *7*, 552–556.
- (30) Karnik, R.; Duan, C.; Castellino, K.; Daiguji, H.; Majumdar, A. *Nano Lett.* **2007**, *7*, 547–551.
- (31) Lev, A. A.; Korchev, Y. E.; Rostovtseva, T. K.; Bashford, C. L.; Edmonds, D. T.; Pasternak, C. A. *Proc. R. Soc. London, Ser. B* **1993**, *252*, 187–192.
- (32) Apel, P. Y.; Korchev, Y. E.; Siwy, Z.; Spohr, R.; Yoshida, M. *Nucl. Instrum. Methods Phys. Res., Sect. B* **2001**, *184*, 337–346.
- (33) Spohr, R. *Radiat. Meas.* **2005**, *40*, 191–202.
- (34) Siwy, Z.; Gu, Y.; Spohr, H. A.; Baur, D.; Wolf-Reber, A.; Spohr, R.; Apel, P.; Korchev, Y. E. *Europhys. Lett.* **2002**, *60*, 349–355.
- (35) Siwy, Z.; Dobrev, D.; Neumann, R.; Trautmann, C.; Voss, K. *Appl. Phys. A* **2003**, *76*, 781–785.
- (36) Siwy, Z.; Apel, P.; Baur, D.; Dobrev, D. D.; Korchev, Y. E.; Neumann, R.; Spohr, R.; Trautmann, C.; Voss, K. -O. *Surf. Sci.* **2003**, *532*–*535*, 1061–1066.
- (37) Siwy, Z.; Apel, P.; Dobrev, D.; Neumann, R.; Spohr, R.; Trautmann, C.; Voss, K. *Nucl. Instrum. Methods Phys. Res., Sect. B* **2003**, *208*, 143–148.
- (38) Siwy, Z.; Fuliński, A. *Am. J. Phys.* **2004**, *72*, 567–574.
- (39) Harrell, C. C.; Siwy, Z.; Martin, C. R. *Small* **2006**, *2*, 194–198.
- (40) Scopece, P.; Baker, L. A.; Ugo, P.; Martin, C. R. *Nanotechnology* **2006**, *17*, 3951–3956.
- (41) Martin, C. R.; Nishizawa, M.; Jirage, K. B.; Kang, M. J. *Phys. Chem. B* **2001**, *105*, 1925–1934.
- (42) Lee, S. B.; Martin, C. R. *J. Am. Chem. Soc.* **2002**, *124*, 11850–11851.
- (43) Harrell, C. C.; Lee, S. B.; Martin, C. R. *Anal. Chem.* **2003**, *75*, 6861–6867.
- (44) Siwy, Z.; Heins, E.; Harrell, C. C.; Kohli, P.; Martin, C. R. *J. Am. Chem. Soc.* **2004**, *126*, 10850–10851.
- (45) Harrell, C. C.; Kohli, P.; Siwy, Z.; Martin, C. R. *J. Am. Chem. Soc.* **2004**, *126*, 15646–15647.
- (46) Nednoor, P.; Chopra, N.; Gavalas, V.; Bachas, L. G.; Hinds, B. J. *Chem. Mater.* **2005**, *17*, 3595–3599.
- (47) Ramírez, P.; Mafé, S.; Aguilera, V. M.; Alcaraz, A. *Phys. Rev. E* **2003**, *68*, 011910.
- (48) Ramírez, P.; Mafé, S.; Alcaraz, A.; Cervera, J. J. *Phys. Chem. B* **2003**, *107*, 13178–13187.
- (49) Alcaraz, A.; Nestorovich, E. M.; Aguilera-Arzo, M.; Aguilera, V. M.; Bezrukov, S. M. *Biophys. J.* **2004**, *87*, 943–957.
- (50) Fuliński, A.; Kosińska, I. D.; Siwy, Z. *Europhys. Lett.* **2004**, *67*, 683–689.
- (51) Siwy, Z. S.; Powell, M. R.; Kalman, E.; Astumian, R. D.; Eisenberg, R. S. *Nano Lett.* **2006**, *6*, 473–477.
- (52) Siwy, Z. S.; Powell, M. R.; Petrov, A.; Kalman, E.; Trautmann, C.; Eisenberg, R. S. *Nano Lett.* **2006**, *6*, 1729–1734.
- (53) Siwy, Z.; Fuliński, A. *Phys. Rev. Lett.* **2002**, *89*, 198103.
- (54) Heins, E. A.; Baker, L. A.; Siwy, Z. S.; Mota, M. O.; Martin, C. R. *J. Phys. Chem. B* **2005**, *109*, 18400–18407.
- (55) Miedema, H.; Meter-Arkema, A.; Wierenga, J.; Tang, J.; Eisenberg, B.; Nonner, W.; Hektor, H.; Gillespie, D.; Meijberg, W. *Biophys. J.* **2004**, *87*, 3137–3147.
- (56) Woermann, D. *Nucl. Instrum. Methods Phys. Res., Sect. B* **2002**, *194*, 458–462.
- (57) Woermann, D. *Phys. Chem. Chem. Phys.* **2003**, *5*, 1853–1858.
- (58) Woermann, D. *Phys. Chem. Chem. Phys.* **2004**, *6*, 3130–3132.
- (59) Cervera, J.; Schiedt, B.; Ramírez, P. *Europhys. Lett.* **2005**, *71*, 35–41.
- (60) Fuliński, A.; Kosińska, I. D.; Siwy, Z. *New J. Phys.* **2005**, *7*, 132.
- (61) Kosińska, I. D.; Fuliński, A. *Phys. Rev. E* **2005**, *72*, 011201.
- (62) Cervera, J.; Schiedt, B.; Neumann, R.; Mafé, S.; Ramírez, P. *J. Chem. Phys.* **2006**, *124*, 104706.
- (63) Lakshminarayanaiah, N. *Equations of Membrane Biophysics*; Academic Press: New York, 1984.
- (64) Robinson, R. A.; Stokes, R. H. *Electrolyte Solutions*; Butterworth Scientific Publications: London, 1955.
- (65) Harrell, C. C.; Choi, Y.; Horne, P.; Baker, L. A.; Siwy, Z. S.; Martin, C. R. *Langmuir* **2006**, *22*, 10837–10843.